Journal of Ocean Engineering and marine Energy manuscript No.
(will be inserted by the editor)

Spatio temporal variability of mean wave energy flux in the Caribbean Sea

Andrés F. Orejarena-Rondón · Juan-Manuel Sayol · Ismael Hernández-Carrasco · Alejandro Cáceres-Euse · Juan C. Restrepo · Alejandro Orfila

Received: date / Accepted: date

Abstract Mean Wave Energy Flux (hereinafter WEF) is assessed in the Caribbean Sea from a 60-year (1958–2017) wave hindcast. We use a novel approach, based on neural networks, to identify coherent regions of WEF and their association with different climate patterns. This method allows for a better evaluation of the underlying dynamics behind seasonal and inter-annual WEF variability, including the effect induced by the latitudinal migration of the Intertropical Convergence Zone (ITCZ) and the influence of El Niño-Southern Oscillation (ENSO) events. Results show regional differences in WEF variability likely due to both intensification and migration of the ITCZ. WEF exhibits a strong semi-seasonal signal in areas of the continental shelf, with maxima reached in January and June, in agreement with the known sea sur-

A. Orejarena-Rondón
Grupo de Investigación en Geociencias GEO4, Departamento de Física y Geociencias, Universidad Del Norte, km 5 Vía Puerto Colombia, Barranquilla, Colombia
E-mail: orejarenaa@uninorte.edu.co

J.M. Sayol
Department of Applied Mathematics, University of Alicante, 03690 Sant Vicent del Raspeig, Alicante, Spain
E-mail: juanma.sayol@ua.es

I. Hernández-Carrasco
Sistema de Observación Costero de les Illes Balears, SOCIB, 07007 Palma de Mallorca, Spain
Mediterranean Institute for Advanced Studies, IMEDEA (CSIC-UIB), 07190 Esporles, Spain

A. Cáceres-Euse
Mediterranean Institute of Oceanography, MIO, Université de Toulon, 83041 Toulon, France

J. C. Restrepo
Dpto. de Física y Geociencias, Universidad del Norte, Puerto Colombia, 081007, Colombia

A. Orfila
Mediterranean Institute for Advanced Studies, IMEDEA (CSIC-UIB), 07190 Esporles, Spain
Tel.: (+34)971611239
E-mail: alejandro.orfila@csic.es

face temperature and sea level pressure variability patterns. At larger scales, WEF shows a significant correlation with the Oceanic Niño Index (ONI, which is the primary index for tracking the ocean part of ENSO climate pattern), depicting positive values in the central and western sides of the basin and negative ones at the eastern side.

Keywords Wave energy flux · Spatio-temporal variability · Caribbean Sea · Self-Organizing Maps · El Niño-Southern Oscillation · wind variability

1 Introduction

The mean wave energy flux (WEF) provides information on the magnitude and temporal variations of the energy transferred from the atmosphere to the ocean over selected periods of time (e.g. months, seasons or even years) (Dodet et al. 2010; Ardhuin and Orfila 2018). It also extracts key details on sea surface waves that may not be detected from single parameters, such as significant wave height (H_s) or wave period (T_{m-01}), becoming a more suitable indicator to capture wave climate variations (Reguero et al. 2019). Long time series of WEF can be used to determine potential impacts on coastal zones, such as variations in the planform of beaches allowing the assessment of eventual impacts of future wave variations on coastal areas (Fiedler et al. 2015; Elshinnawy et al. 2017). Additionally, ocean waves are one of the renewable energy resources that has attracted more attention in the last years due to its potential capability of providing green and sustainable electricity offering several advantages with respect to other energy resources (Lin et al. 2019; Arinaga and Cheung 2012; Liang et al. 2017). Therefore a precise characterization of the spatial and temporal variability of WEF is crucial to evaluate the local and regional impact of the evolving wave climate in the context of the ongoing global warming (Wiggins et al. 2019; Elshinnawy et al. 2017; Hanson et al. 2003). However, due to the scarcity of wave measurements around the world, to get the spatio temporal distribution of WEF we need to use validated wave hindcasts provided by numerical models (Mentaschi et al. 2017; Mirzaei et al. 2015; Waters et al. 2009; Iglesias et al. 2009).

Previous studies have analyzed inter-annual and long-term WEF variations associated with climate indices (e.g., El Niño-Southern Oscillation (ENSO), Pacific Decadal Oscillation (PDO), Tropical North Atlantic index (TNA)) and climate change projections, respectively. On a global scale, Reguero et al. (2019) found from a 60-year wave reanalysis that wave power has increased at a rate of 0.4% per year at global scale. These results indicate that the anthropogenic global warming is strengthening synoptic winds in some regions, thus favoring the generation of larger surface waves and affecting the global wave climate. Reguero et al. (2015) characterized the mean wave power globally as well as its seasonal variability with a global wave reanalysis performed with WAVEWATCH III model. Their results showed that the effect of the interannual variability is more prominent over the Northern Hemisphere, where the

contribution of the seasonal variability is larger. Wu et al. (2017), used ERA-Interim wave reanalysis data for the period 1997–2010 to evaluate WEF trends at global scale, as well as trends of time series of simple parameters such as the significant wave height (H_s), mean wave period (T_{m-01}), and wave direction (θ_m). Among the studied parameters, they found a significant increase in the magnitude of WEF, H_s and T_{m-01} in southern mid-latitudes and in the western part of the North Atlantic and of the North Pacific. In contrast, they found a significant decrease of the same parameters in the eastern part of the tropical North Pacific (Wu et al. 2017). Mentaschi et al. (2017) analyzed global trends of extreme WEF along global coastlines during the 21^{st} century under a high emission scenario, RCP 8.5 (Representative Concentration Pathways delivering global warming at an average of 8.5 W/m^2 across the planet). Results for this pessimistic projection would imply a WEF increase of up to 30% for most of the southern mid-latitudes, while in the Northern Hemisphere many coastal areas displayed negative trends. They also showed that significant long-term trends in the extreme WEF are related with the intensification of inter-annual signals such as El Niño-Southern Oscillation (ENSO) and the North Atlantic Oscillation (NAO). On regional and local scales, several dedicated model-based studies have been developed to evaluate the wave energy resource, either the spatial distribution or the temporal variability (Liberti et al. 2013; Ponce de León et al. 2016; Liang et al. 2017; Canals Silander and García Moreno 2019; Cuttler et al. 2020; Guillou et al. 2020), which have helped to improve the design and deployment of wave energy converters in the study areas. Previous studies have already characterized the wave power in the Caribbean sea. Ortega et al. (2013) identified the best sites for a wave farm near the small island of Isla Fuerte by means of numerical simulations. Osorio et al. (2015) assessed the wave power potential in the Colombian Caribbean showing that the highest values of mean wave power are of 5–7 kW/m from December to April. This potential is relatively small compared to other places around the world, where powers of about 40 kW/m and above are considered profitable to implement wave farms. Appendini et al. (2015) studied the wave energy potential in the whole Caribbean Sea from a 30-year wave reanalysis detecting that below the influence area of the Caribbean Low Level Jet (CLLJ), in the central Caribbean, the amount of wave power presents values between 8 – 14 kW/m. They also mentioned the existence of large spatial wave power gradients, which need to be considered for the installation of energy extraction devices. Guillou (2020); Guillou et al. (2020) recently analyzed the wave energy and wave power resources for the whole North Atlantic, including the Caribbean Sea, using wave buoys at the open sea and a 30-year reanalysis, respectively. Several metrics were compared to quantify the useful wave energy, as well as its seasonal variability. The maximum WEF was found during late fall (December and January) and late spring (June and July) with wave power ranges in the Caribbean Sea within the range of previous studies (5 – 14 kW/m).

Recently, with the same simulation we use in this work Orejarena-Rondón et al. (2022) analyzed WEF trends in the Caribbean Sea, showing a decrease

between 1958–2017 with an annual rate that oscillates between 0.01% and 0.2%, depending on the region. They also pointed out the necessity of further studies on the WEF variability to analyze the changes in the coastal zones as the result of the incident angle to the coast, as well as to identify potential coastal areas suitable for deploying efficient and cost-effective wave energy converters. From this perspective, here we go one step further to analyze the spatial and temporal variability of WEF in the Caribbean Sea from 1958 to 2017 using a novel approach with which coherent regions that show similar WEF are distinguished according to their associated wind pattern. By applying this method one gets new insights on the physical processes that drive seasonal and inter-annual WEF changes, including the impact of ITCZ migration and ENSO events.

The article is structured as follows: the main Caribbean Sea features are described in section 2. Data set and methods are outlined in section 3. Section 4 shows the main results including model validation, regional characterization of WEF and surface wind, as well as their temporal variability at seasonal and inter-annual scales. Finally, in section 5 we discuss the main results in the context of the current literature, and the main conclusions are outlined.

2 Study area

The Caribbean Sea is located between latitudes 8.1°N – 13.6°N and longitudes 84.52°W–59.7°W, being bordered by the Lesser Antilles at the east, the Greater Antilles at the north, the eastern portion of Central America at the west and the northern coasts of South America at the south (Figure 1). Wave dynamics is mainly controlled by the westward surface trade winds, which show a large seasonality, and a low-level wind core with higher speeds that gives origin to the Caribbean Low Level Jet (CLLJ). The CLLJ has its kernel at a height of around 925 hPa, although can reach heights over 800 hPa and is located in the center of the basin (Amador 1998; Poveda and Mesa 1999; Poveda et al. 2006; Chunzai 2007; Orfila et al. 2021). Wind seasonality is associated to the meridional migration of the ITCZ, which is also responsible for the path and penetration of transient features as cold fronts and tropical storms (Poveda et al. 2006; Poveda 2004; Andrade and Barton 2013). The meridional oscillation of the ITCZ responds to the seasonal insolation cycle. During the austral summer the ITCZ is located between Colombia and Ecuador, whereas it shifts northward in the boreal summer. When the ITCZ is located between 0–5°S, the northern trade winds dominate in these regions with an average speed that varies between 8 and 15 m/s (Andrade 1993; Orfila et al. 2021; Sayol et al. 2022). This seasonality is modulated by regional sea surface temperature and sea level gradients which add a semi-seasonal component (Chunzai 2007).

Regarding atmospheric instability conditions, there is little rainfall from December to April over the Colombian basin and in the west of the Antilles. Conversely, in the Caribbean coasts surrounding the Gulf of Darien (which

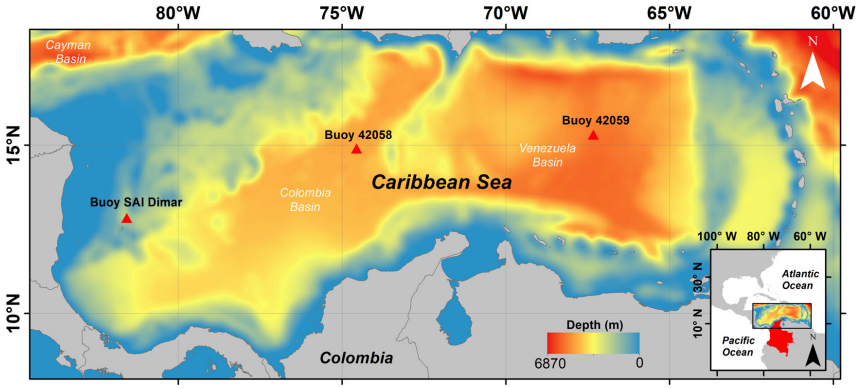

Fig. 1 SWAN domain used for the 60-year wave simulation in the Caribbean basin. Red triangles indicate the location of buoys used for the validation: Buoy SAI DIMAR, NOAA buoy 42058, and NOAA buoy 42059, ordered from west to east.

includes coasts of Colombia, Panamá and Costa Rica), it rains throughout almost the whole year (Andrade et al. 2013). By contrast, when the ITCZ is located at a latitude between 10–12°N, from August to November, the weaker southern trade winds (with a mean speed of ∼4 m/s) reach the Colombian basin, contributing to the formation and even strengthening of tropical convective storms that may reach hurricane category over the western Caribbean Sea (Andrade et al. 2013). As a result, the precipitation caused by the displacement of the ITCZ only affects the Colombian basin below 10°N. Consequently, trade winds (and hence the CLLJ) permanently remain above La Guajira peninsula. The rest of the year there is a transition period between the aforementioned seasons, in which trade winds weaken and some rainfall comes over the Colombia basin from April to June, while from June to August trade winds strengthen and rainfall decreases. The latter transition time is locally known as "Veranillo de San Juan" from its name in Spanish (Poveda et al. 2006; Andrade et al. 2013). Winds and rainfall are sensitive to the arrival of oscillations such as easterly waves, with periods of 7 days, and cold fronts, coming from North America and crossing the Caribbean towards the east in about 10 to 14 days generating precipitation and rising wind stress on its way (Andrade et al. 2013; Alvarez-León et al. 1995). Large-scale signals such as the Madden-Julian Oscillation have longer periods (40 to 50 days) and have been detected in sea surface temperature and in rainfall records in Santa Marta, Colombia, at a latitude above 11°N (Rivera-Páez and Molares 2003; Andrade et al. 2013). Moreover, there is also a strong inter-annual variability associated with ENSO that affects both Atlantic and Caribbean coastal areas. Huang et al. (2002); Enfield and Mayer (1997); Sayol et al. (2022) determined that at the end of the year, when El Niño tends to become stronger, trade winds weaken over the eastern Caribbean Sea at a latitude between 10°N and 20°N, extending until Africa. In contrast, in the western part of the Caribbean Sea trade winds strengthen during El Niño events.

3 Data and Methods

3.1 Wind data

Surface wind fields used to force the Simulating WAves Nearshore (SWAN) model in the study area correspond to the Japanese 55-year Reanalysis (JRA-55) simulation performed by the Japan Meteorological Agency. This data was the first complete reanalysis in covering the last half century, and was later extended until the near-present (1958–2020), being also the first one that applied a four dimensional variational analysis (Kobayashi et al. 2015). This set of global atmospheric data is suitable to study multidecadal variability and the relation of wave climate with climate change (Japan Meteorological Agency 2013). Output fields provide the 10 m height wind speed (u_w, v_w) on a mesh of 23 × 43 grid points with a spatial resolution of 0.5625° × 0.5616°. The data cover the whole study area from 84.3746°W, 7.5819°N (lower left corner) to 60.1871°W, 19.9371°N (upper right corner) from 1958–2017 (both included) with a 3-hourly temporal resolution.

3.2 Simulated WAve Nearshore-SWAN Model

The SWAN model solves the wave action balance equation for the propagation of the wave spectrum, which allows for realistic estimations of wave parameters in the open ocean and coastal areas (Booij et al. 1999). The SWAN domain covers an area of 2600 km × 1175 km distributed into 229 × 101 grid cells (Figure 1). The bathymetry of the Caribbean Sea was obtained from Colombian Hydrographic Service nautical charts as well as from the general ocean bathymetric chart (GEBCO). Waves were simulated in non-stationary mode using the JRA-55 wind fields. Wind-induced wave growth was configured as exponential following the formulation of Komen et al. (1984), while nonlinear deep water interactions were parameterized following the *Webb-Resio-Tracy* method (van Vledder 2006). Other relevant processes, such as wave breaking, white capping energy dissipation, and bottom friction were included in the simulations. The integration time step was set as 30 minutes and $\mathrm{H_s}$, $\mathrm{T_{m-01}}$, and θ_m output data were recorded every 3 hours in each domain grid cell. $\mathrm{H_s}$ and $\mathrm{T_{m-01}}$ were validated through a comparison with in situ wave data measured by the NOAA-42058 buoy, which is located in the central Caribbean Sea (Figure 2). The wave reanalysis we use in this work is published in Orejarena-Rondón et al. (2021). To calculate error parameters between the data of the buoys and SWAN results, we used Willmott's index D, the average bias (P) index and the Pearson correlation (Ortiz-Royero and Mercado-Irizarry 2008). Willmott's index was calculated as:

$$D = \frac{\sum_{n=1}^{N}(P_n - O_n)^2}{\sum_{n=1}^{N}(|P_n - O| + |O_n - O|)^2} \quad (1)$$

While the bias index was calculated as:

$$D = \frac{\sum_{n=1}^{N}(P_n - O_n)}{\sum_{n=1}^{N}(O_n)} \quad (2)$$

In both equations N is the number of evaluated values, P_n are the predicted values, O_n are the observed data and O is the mean value of the data. When Willmott's index equals to 0 indicates complete disagreement, while when it equals to 1 indicates a perfect agreement. Regarding the bias index, when it equals to 0 indicates a perfect agreement, while a bias of -0.05 indicates that the predicted data underestimates the observed data by 5%.

The Pearson correlation was calculated as:

$$r_{(x,y)} = \frac{cov(X,Y)}{\sigma_X \sigma_Y} \quad (3)$$

Where cov is the covariance, σ_X and σ_Y are the standard deviations of X and Y, respectively. A value of the Pearson index of 1 indicates a perfect agreement. Besides, the p_value indicates if the relationship is statistically significant at a given confidence interval. For instance, a $p\_value < 0.05$ indicates that the relationship has a 95% confidence level for a two-tailed t-Student distribution (0.025 in each tail).

3.3 Wave Energy Flux (WEF) calculation

Departing from the 3-hourly SWAN model output fields ($\mathrm{H_s}$, $\mathrm{T_{m-01}}$, θ_m), the monthly mean WEF was determined for the period 1958 – 2017. The WEF ($\mathrm{FE_x}, \mathrm{FE_y}$) was computed as:

$$\overrightarrow{\mathrm{FE}} = \frac{1}{64\pi}\rho g^2 T_{m-01} {H_s}^2 \frac{\overrightarrow{k}}{|\overrightarrow{k}|} \quad (4)$$

where ρ is the seawater density in $\mathrm{kg/m^3}$, g is the gravity acceleration, $\mathrm{T_{m-01}}$ is the mean period, $\mathrm{H_s}$ is the significant wave height and $\overrightarrow{k}$ is the wavenumber vector. Departing from these components, we carried out a spatial and temporal characterization of the mean WEF in the Caribbean basin through a Self-Organizing Map analysis. Similarly, we have analyzed the inter-annual variability of the monthly mean WEF over time through a correlation analysis with ENSO indices.

3.4 Self-Organizing Map (SOM)

Self-Organizing Map is a statistical tool used to compress the information contained in a large amount of data into one single set of maps (Kohonen 1982), reducing the high dimensional feature space of input data to a lower dimensional network of units called neurons. This unsupervised learning neural network is able to extract patterns from large data sets mimicking the topological distribution of the brain neurons response in the brain. The SOM analysis has been used in the oceanography context in several studies (Richardson et al. 2003; Hernández-Carrasco and Orfila 2018; Hernández-Carrasco et al. 2018; Morales et al. 2022). However, to our knowledge applications of SOM analysis have not been addressed in order to obtain regional patterns in the Caribbean Sea of coherent wave energy flux variability.

Learning processes are carried out by an interactive presentation of the input data to a preselected neuronal network, which is modified during the iterative process. Each unit is represented by a weight vector with a number of components equal to the dimension of the input data. During each iteration, the neuron whose weight vector is the closest to the presented sample input data vector, called Best-Matching Unit (BMU), is updated together with its topological neighbors towards the input sample (see Hernández-Carrasco and Orfila (2018) for a more detailed description of the SOM process). When the probability density function of the input data is approximated by SOM, and each unit is associated with that reference pattern that has a number of components equal to the number of variables in the data set, the training process finishes. Thus, this process can be interpreted as a generalization of similar observations. In this study, a joint SOM analysis is applied over the monthly mean fields of both WEF and surface wind in the area covered by the 60-year wave reanalysis. In the case of the spatial analysis, since each iteration is associated to a given time and a location of the sample, one can obtain the evolution of a particular pattern computing the BMU for each sample. In the temporal domain the analysis of the neurons provides temporal patterns and the BMU is used to localize in space the temporal variability, identifying regions of similar co-variability patterns.

The size of the neural network is an important parameter to take into account in order to maximize the quality of the SOM analysis. The determination of the size of the neural network is empirical and somehow subjective (Morales-Márquez et al. 2021). We chose the number of neurons of the network after testing several sizes of the map to check that the cluster structures are shown with sufficient resolution and statistical accuracy. In our case we have selected for both temporal and spatial patterns 3×3 neurons since this number facilitates the interpretation of the patterns without loosing variability of the data set. In all of them, we have chosen the same number of rows and columns (square network) in order to make easier the identification of the transition between groups of patterns. Due to the preservation of topology, similar patterns are ordered according to the similarity and the resulting groups of patterns are located around the four corners of the network (Hernández-Carrasco et al.

2020). To analyze the effect of using different sizes of the neural networks in the SOM computations, we have compared the results for three sizes: 2×2, 4×4, and 6×6. Sizes larger than 6×6 result in an unfeasible neural network since the large number of neurons does not allow to identify any pattern. For 2×2 neurons, obtained patterns are too coarse and there is a loss of variability since transition patterns do not appear, which may potentially result in the lack of the insights of the wave energy flux patterns evolution. In contrast, for 6×6 neurons, obtained patterns are hard to read because of the large number of patterns with zero probability of occurrence. For the 3×3 SOM analysis we found the optimal representation of the variability of patterns with nonzero probability of occurrence, showing negligible differences with the 4×4 neurons. Note that patterns with zero probability of occurrence are included by the algorithm to preserve the topology.

3.5 Correlation and Cross Wavelet Transform Analysis

To explore the link between monthly mean WEF and ENSO at inter-annual scales we have proceeded as follows. First, we have performed a direct correlation analysis between the Oceanic Niño Index (ONI) and the monthly mean WEF time series at every grid cell within the study area (Figure 12); second, the cross wavelet transform (XWT) and wavelet coherence (WTC) analysis are applied on the ONI index and the time series associated with each of the 9 regions determined by SOM. The XWT between the temporal signals of the mean WEF and ONI reveals those regions where energy variance is more correlated, also giving information about their phase relationship. The XWT of any two time series x_n and y_n is defined as $W^{XY}(s) = W^X(s)W^{Y*}(s)$, where $*$ denotes the complex conjugate and s is the time scale. Furthermore, the cross wavelet power is defined as $|W^{XY}(s)|$ and its complex argument as $\arg(W^{XY}(s))$. The latter represents the relative local phase between x_n and y_n, which we will depict by arrows. The WTC spectrum highlights how large is the covariance of these signals, regardless of the high power display (Grinsted et al. 2004; Nalley et al. 2016; Restrepo et al. 2019). The degree of coherence of XWT is given by the following coefficient:

$$R_n^2(s) = \frac{|S(s^{-1}W_n^{XY}(s)|^2}{S(s^{-1}|W_n^X(s)|^2) \cdot S(s^{-1}|W_n^Y(s)|^2)}, \tag{5}$$

where S is a smoothing operator with values ranging between 0 (no correlation) and 1 (perfect correlation). The relationship between WEF and ONI is identified by the phase angle observed in the spectrum. An in phase relationship is indicated by the arrows pointing to the right. On the other hand, an out of phase relationship is indicated by arrows pointing to the left. Arrows that do not point straight to the right or to the left indicate a lagged correlation relationship.

4 Results

4.1 Wave model validation

Validation of SWAN simulation is performed with the NOAA buoy 42058, which is located in the central Caribbean Sea, using both H_s and T_{m-01} (see Figure 1). Conversely, due to the unavailability of other parameters, only modeled H_s can be validated with those buoys located near of San Andres Island: Buoy SAI Dimar and NOAA buoy 42059, which are located at the west and east sides of the basin, respectively (see Figure 1). In the case of the buoy NOAA-42058, a good fit between *in-situ* and model data was obtained. For H_s, bias, correlation, and Willmot coefficient, we get values of 0.064, 0.83, and 0.9, respectively; while for T_{m-01}, bias, correlation, and Willmot coefficient yield values of 0.089, 0.74 and 0.77, respectively (Figure 2). For the other two

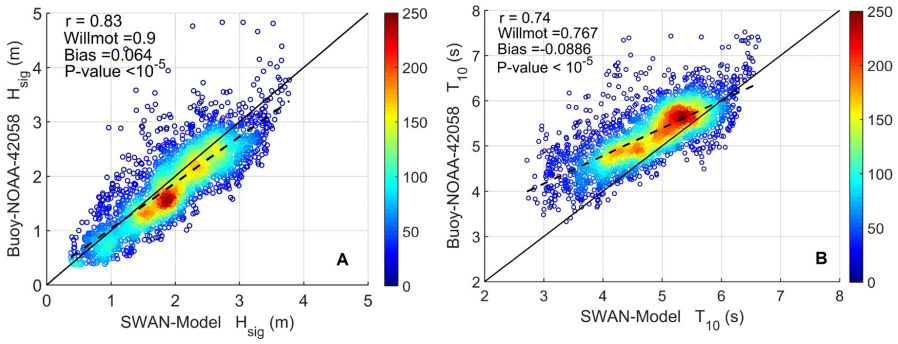

Fig. 2 Validation of: (A) significant wave height (H_s), and (B) wave period (T_{m-01}) in the central Caribbean Sea between SWAN simulation and observations provided by buoy 42058 (Figure 1). Color scale of dispersion diagrams corresponds to associated density of data used for validation. The linear regression is represented by a black dashed line.

buoys, a good fit was found between modeled H_s and *in-situ* H_s estimates. Correlation coefficients for buoy NOAA 42059 and buoy SAI Dimar were 0.7 and 0.91, respectively (Figure 3). Willmot coefficient values were 0.822 and 0.974 for buoy NOAA 42059 and buoy SAI Dimar, respectively, while bias coefficients for buoy NOAA 42059 and buoy SAI Dimar of 0.03 and 0.0034, respectively.

4.2 Characterization of mean WEF and surface wind in the Caribbean Sea

Monthly mean and standard deviation of WEF and surface wind are shown in Figure 4 (A-B and C-D, respectively). The large mean wind speed is reflected in the intensification of the CLLJ over approximately 68°W to 80°W and between 12°N and 16°N, with average speeds between 8 and 10 m/s. Wave

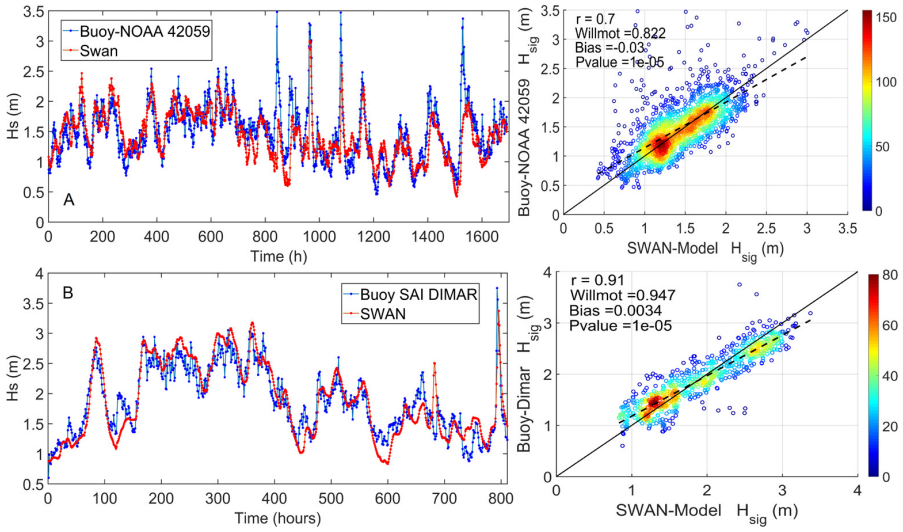

Fig. 3 Validation of H_s in the west and east of Caribbean basin (see buoys SAI DIMAR and NOAA 42059 locations in Figure 1, respectively). Color scale of dispersion diagrams corresponds to associated data density used in the validation. The linear regression is depicted by a black dashed line.

response to this forcing is shown in Figure 4A, where WEF starts to rise dramatically at about 70°W and then extends toward the west of the basin. As the WEF is related with the wave height and the period, when the WEF reaches the highest values (1400 W/m, between 75°W and 78°W), wind waves are completely developed. The standard deviation of both mean wave energy flux and wind fields in the study area are shown in Figures 4B and D. The largest deviation for the mean WEF is obtained between 75°W-80°W and 12°N-16°N, whilst for wind speed this is obtained between 73°W-80° W and 10°N-13°N.

4.3 Spatial patterns of monthly mean WEF over the Caribbean Sea from SOM Analysis

As mentioned above, spatial patterns are obtained by applying a joint SOM analysis between the monthly mean WEF and the monthly mean horizontal surface wind fields. The analysis is restricted to the Caribbean Sea and covers the period between 1958 and 2017. Figure 5 (first set of 3×3 neurons, i.e., nine upper sub-figures) and Figure 6 (first set of 3×3 neurons, i.e., nine upper sub-figures), show the coupled patterns obtained from the 3×3 SOM neurons of WEF and surface winds with their corresponding probability of occurrence, which indicates how often these specific patterns occur over the 60 yr. In Figure 5 (nine lower sub-figures) and Figure 6 (nine lower sub-figures)

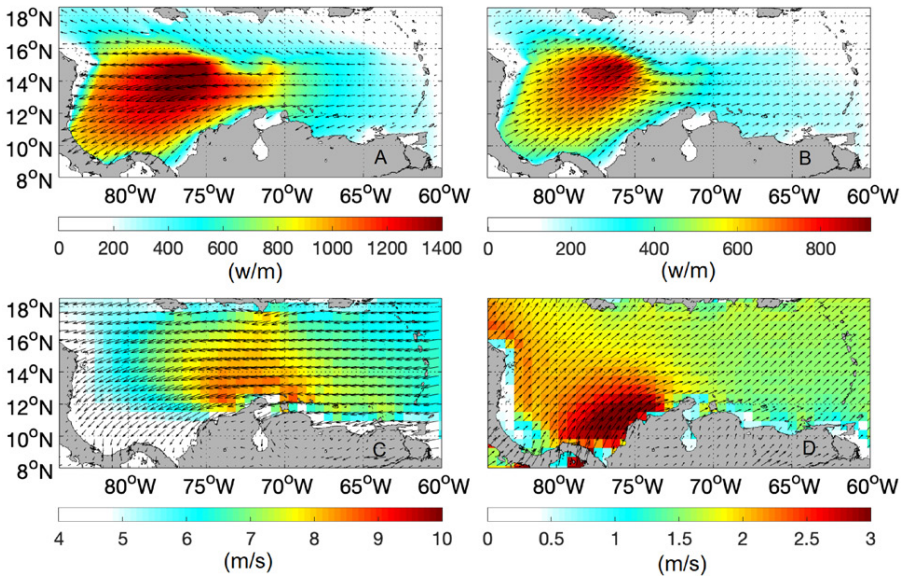

Fig. 4 (A)-(C) Mean wave energy Flux (WEF) and wind field used in the simulations, respectively. (B)-(D) Standard deviation of both mean WEF and wind fields. Background color indicates the magnitude of WEF (in W/m, top panels) and wind speed (in m/s, bottom panels), respectively and the arrows their direction.

the corresponding anomalies are shown for every neuron. Moreover, Figure 7 shows the monthly frequency of occurrence of the patterns determined by the best matching unit (BMU). The BMU is obtained comparing all patterns (1–9) with each sample of the mean WEF to calculate the frequency of occurrence and select the pattern more similar to the sample. All patterns shown in the nine upper sub-figures (Figures 5 and 6) are restricted to a common area in the western Caribbean Sea strongly influenced by the CLLJ. Patterns with the largest probability of occurrence (P1, P6 and P7) are associated with the meridional migration of the ITCZ throughout the year (Figure 7). P1, with an occurrence of 22.6%, is associated with the dry season (December to April, see Figure 7), with the highest probability occurring from January to March (>35%). P7, with an occurrence of 14.6%, is associated with the transition season. This pattern is presented with a low frequency of occurrence during May and August, and with high frequency during June and July (>35%), when the "Veranillo de San Juan" occurs. P6, with an occurrence of 10.4%, is associated with the wet season (from August to November). The highest probability of occurrence of this pattern is presented during the months of September and October (>35%). This pattern also appears in May, a month that corresponds to the transition period, but with lower frequency (15%). Although with less probability of occurrence, other patterns (P2, P3, P4, P5, P8 and P9) also take place in any of the three climatic seasons. For instance, P2 and P4, with

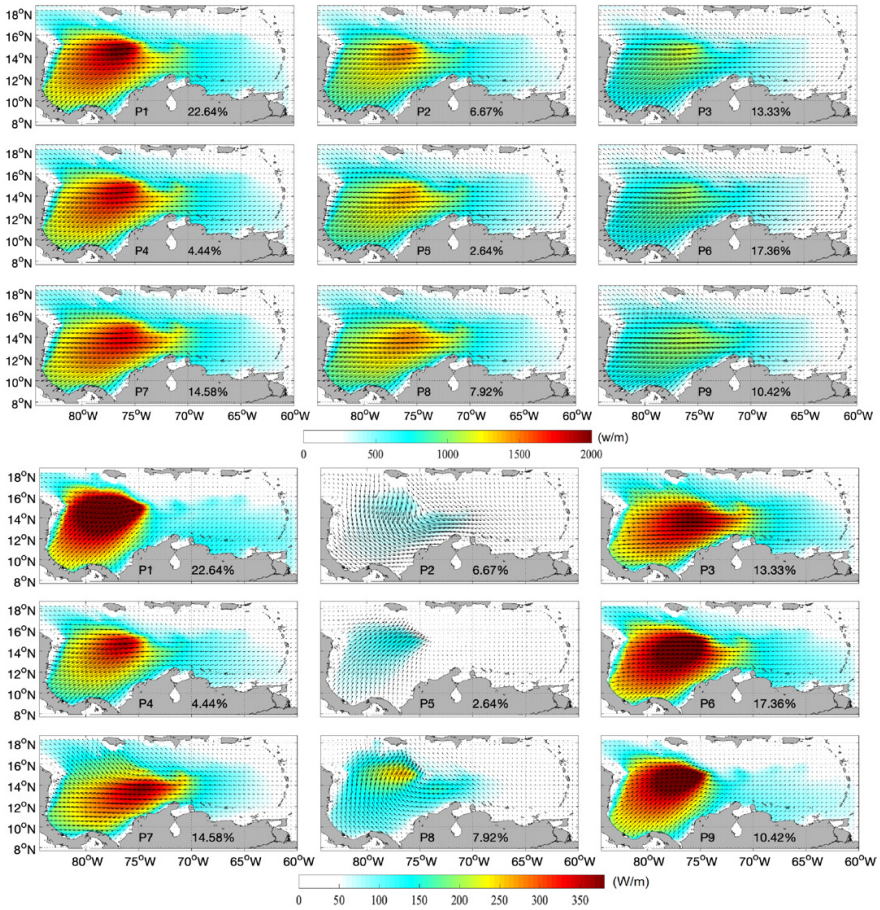

Fig. 5 Spatial patterns of mean wave energy flux (WEF) given by a 3 × 3 SOM analysis with their direction in the Caribbean basin (top panel). Standard deviation for the above mentioned spatial patterns (bottom panel). The percentage shown in each pattern reflects its total occurrence probability in %.

6.7% and 4.4% probability of occurrence, have a low frequency during the dry season (March, April, May and December). P5 and P8, with 2.6% and 7.9% probability of occurrence each one, are associated with the transition season. P9, with 10.4% probability of occurrence, is associated with the wet season (low frequency during June and October and moderate one during May, August and September). P3, with 13.3% probability of occurrence, is presented randomly throughout the year (see Figure 7): the highest probability takes place in November (30%), the intermediate one in April and December (20%), and the lowest one in February and March (10%). In order to assess the spatial and temporal changes of both WEF and surface wind fields we have computed the standard deviation of every SOM pattern (Figure 5 for the WEF and Figure 6 for the wind). Those patterns with the largest variability are P1, P6

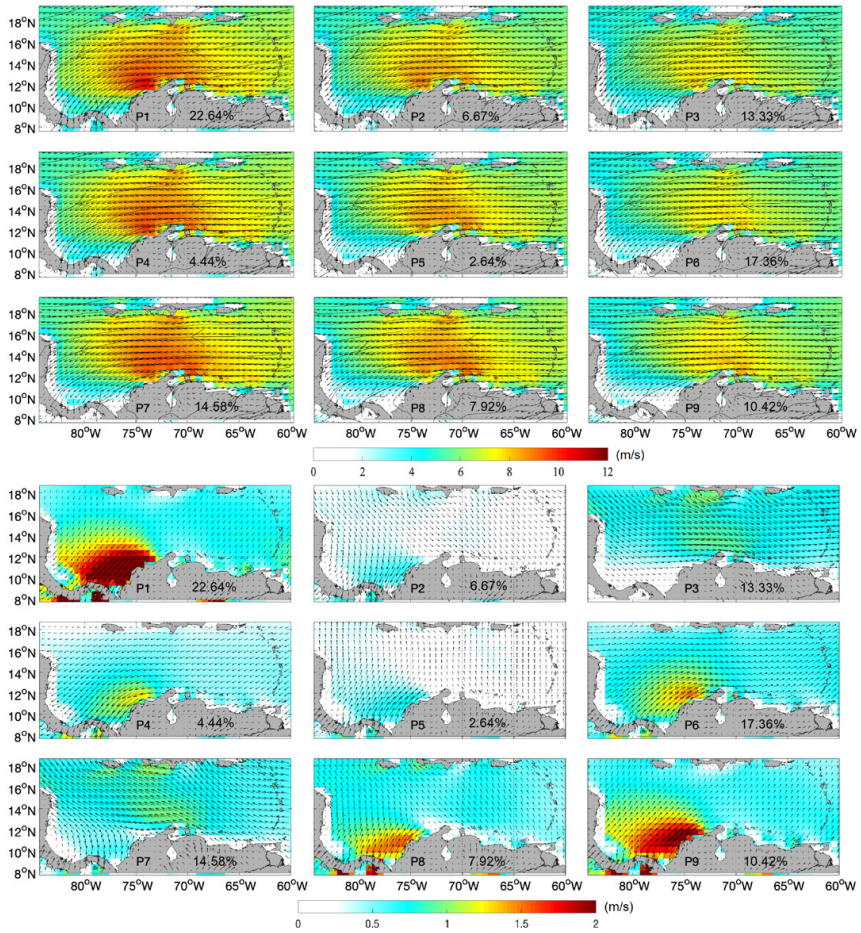

Fig. 6 Spatial patterns of wind fields obtained from the SOM analysis given by a 3 × 3 with their respective direction, in the Caribbean basin (top panel). Standard deviation for the computed above mentioned spatial patterns (bottom panel). The number depicted at the bottom-right in each pattern corresponds with total occurrence probability in %.

and P9 for WEF, and P1 and P9 for wind, being in all cases restricted to the western Caribbean basin. As observed, the increase in the magnitude of the WEF and wind speed, are the result of both the latitudinal displacement of the ITCZ and the intensification of trade winds.

4.4 Temporal patterns of WEF over the Caribbean Sea from SOM analysis

To better explore the dominant direction of WEF, we have applied a temporal SOM analysis over zonal (F_x) and meridional (F_y) components of monthly mean WEF. As we use 3 × 3 neurons again, this analysis also provides 9 zones of co-variability in the Caribbean Sea (Figure 8). Figure 9 shows time

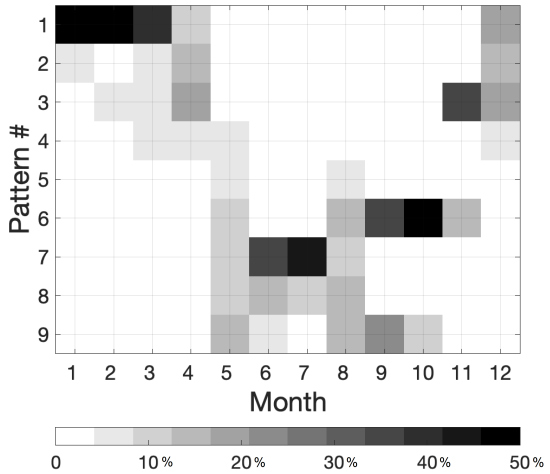

Fig. 7 Seasonal occurrence probability of each spatial pattern of mean WEF and surface horizontal wind fields shown in Figure 5 and Figure 6.

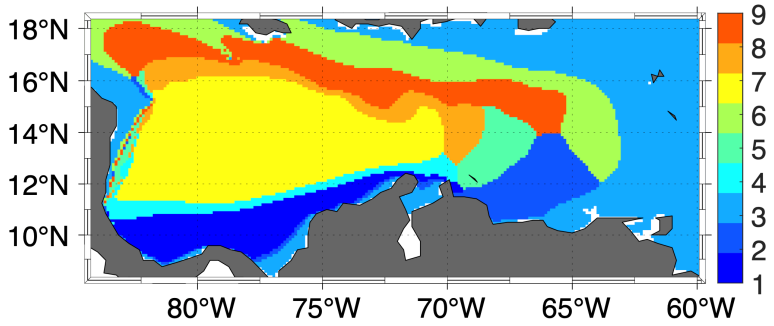

Fig. 8 Regions given by the temporal SOM analysis. SOM was applied with 3×3 neurons over the monthly mean WEF. We refer for these patterns to Figure 9 and Figure 10.

series of F_x and F_y components for every region in top and bottom panels, respectively. The sign $(+/-)$ in the abscissas provides the direction of each component: a negative value indicates a direction towards the west in the zonal component and towards the south in the meridional component, whereas a positive value indicates a direction towards the east in the zonal component and towards the north in the meridional one. Most of the time series conserve the same sign, which allows to clearly identify the dominant direction. As seen, the zonal component is generally twice larger than the meridional one. According to the magnitude of WEF, we can distinguish three groups of zones: the largest values (in absolute magnitude) are observed in zones 7, 4, 1 (in descending order), located in the center and western areas of the Caribbean Basin, from 70°W, extending toward the south and to the west of the basin (Figure 8). Time series of WEF associated with zone 7 (Tp7 in top and bottom panels) reach values between -1300 and -400 (W/m) for F_x, and between -220

and 0 (W/m) for F_y (Figure 9), which indicates that WEF is predominantly oriented towards WSW-W over the 60 years. Similar results are found in zone 4, but with a stronger meridional component. In contrast, zone 1 shows weaker, and slightly turned to the south components (oriented SW-WSW). Moderate values of WEF are observed in zones 8, 5 and 2. These regions cover the center Caribbean basin between 64°W and 70°W, and extend toward the zone 7 (Figure 8). In zone 8, time series of u and v components take values between -1000 and -350 (W/m), and between -60 and 100 (W/m), respectively (Figure 9). It indicates that WEF is predominantly oriented toward the W. Similarly, components in zone 5 are also mainly oriented westward, with values between -850 and -300 (W/m) and between -100 and 40 (W/m) (Figure 9).

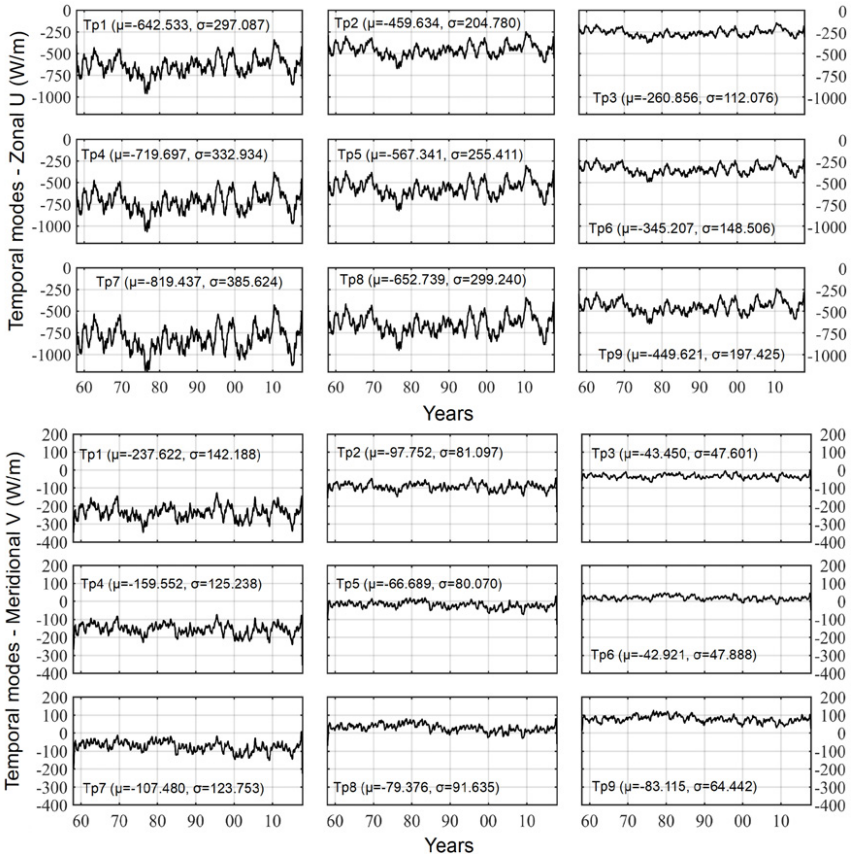

Fig. 9 Temporal patterns provided by a 3 × 3 SOM time domain analysis computed over the monthly mean WEF for zonal (F_x) and meridional (F_y) components (top and bottom panels, respectively). Names on the top-left side of every panel: Tp1, Tp2, ..., Tp9 refer to patterns shown in Figure 8. μ and σ are the mean and the standard deviation of every time series, respectively. Unit in W/m.

Components of zone 2 show weaker zonal values, ranging from -700 and -250 (W/m), and a stronger meridional component, between -240 and -40 (W/m), which is reflected in a slightly turned to the south dominant orientation (WSW). Finally, the lowest values of WEF are observed in zones 9, 6 and 3, which are located at latitudes above the zone 8, in the eastbound of the basin, and off the coastal zones of Colombia, Venezuela and Nicaragua (Figure 8). Time series of F_x and F_y in zone 9 show values between -650 and -250 (W/m) and between 20 and 140 (W/m), respectively (Figure 9). The latter depicts a predominant WNW-W orientation. Similarly, time series of zone 6, with values between -500 and -200 (W/m) and between -40 and 60 (W/m) for u and v, respectively (Figure 9), show a dominant W-WNW orientation. As occurred in zones 5 and 4, components are also slightly turned southward in zone 3, with values between -400 and -150 (W/m) and between -80 and 0 (W/m) for u and v, respectively (Figure 9), with a predominant W-WSW orientation.

4.5 Analysis of WEF direction at seasonal scale

Departing from the time series of Figure 9 we study the direction of mean WEF at a seasonal scale for the 9 zones depicted in Figure 8. To obtain the annual cycle we compute the 60-year monthly mean for each zone and component (Figure 10). Results illustrate a semi-seasonal signal in the zonal component of all regions characterized by two peaks. These peaks take place in January and June (see the most negative values), while the minimum values (in magnitude) are reached in April and September. These relative extremes are associated to the latitudinal migration of the ITCZ, which affects the magnitude of the trade winds. Regarding the meridional component, we find a mixed behavior: Zones 1, 2 and 4 also show two peaks (see Figure 10, bottom panel), while in northern regions such (Zones 6, 8 and 9) there is only one peak, which takes place in May. Figure 11 summarizes previous results showing the resultant 60-year monthly mean direction of WEF for every pattern shown in Figure 8. As seen above, the largest WEF (>1000 W/m) comes from east and east-northeast and correspond to patterns P7 and P4. Other modes such as P2, P3 and P9 represent weaker configurations (100-500 W/m), although waves keep coming from east-northeast or east-southeast, thus depicting small fluctuations in the direction throughout the year. This small variation in the direction is expected from the dominant trade winds.

4.6 Relationship between ENSO and the inter-annual variability of WEF

To evaluate the influence of ENSO on the inter-annual variability of WEF we have performed a correlation analysis between both variables. To this end, we use monthly time series of ONI and monthly mean WEF spanning from 1958 to 2017 (both years included). Results show relatively large simultaneous correlations (of about $r = 0.4$) between the mean WEF and the ONI

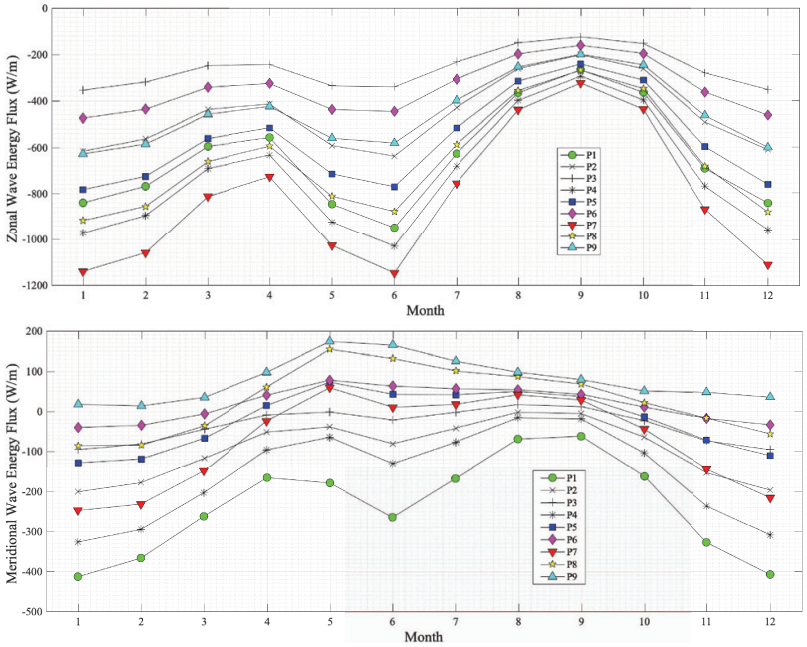

Fig. 10 60-year monthly mean WEF zonal (top panel) and meridional (bottom panel) components. Units in (W/m).

off the Caribbean coasts of Colombia and in the central Caribbean Sea, at latitudes between 11°N and 17°N and longitudes between 70°W and 77°W (Figure 12). Lower positive correlations ($r \in [0.1, 0.2]$) are found at latitudes between 10°N and 17°N, and at longitudes between 77°W and 85°W. Conversely, negative correlations ($r \in [-0.3, -0.1]$) are observed off Venezuela coasts, in the southeastern Caribbean basin (Figure 12). Next, we have computed the wavelet coherence (WTC) for all zones provided by the temporal SOM decomposition. The results show that ENSO correlates well and coherently with the mean WEF over a long range of time scales and frequencies (Figure 13). Additionally the spectrum reveals a strong co-variability between ENSO and WEF in all regions for periods ranging from 24 to 32 months, and from 32 to 64 months. The longest period with significant correlation corresponds to 74 months ($\geq$ 6 years). The relative phase indicates that ENSO leads WEF by 45° at periods between 32 and 64 months, and by 90° for periods between 64 and 72 months in all regions (see arrows in Figure 13 pointing downward). For example, for periods between 32 and 64 months WTC revealed a lag (ENSO leads) during 1993 and 1999 in all zones (see the large coherence during El Niño 1998). Moreover, there is a longer lag (ENSO leads) during 2001 and 2011 for regions 4–9. The WTC also reveals a significant coherence between ENSO and mean WEF for periods between 24 and 40 months, as well as an increase in the coherence for periods between 24 and 92 months at the end of the two series, mainly in regions 1, 4 and 7 (Figure 13A-C, respectively). The

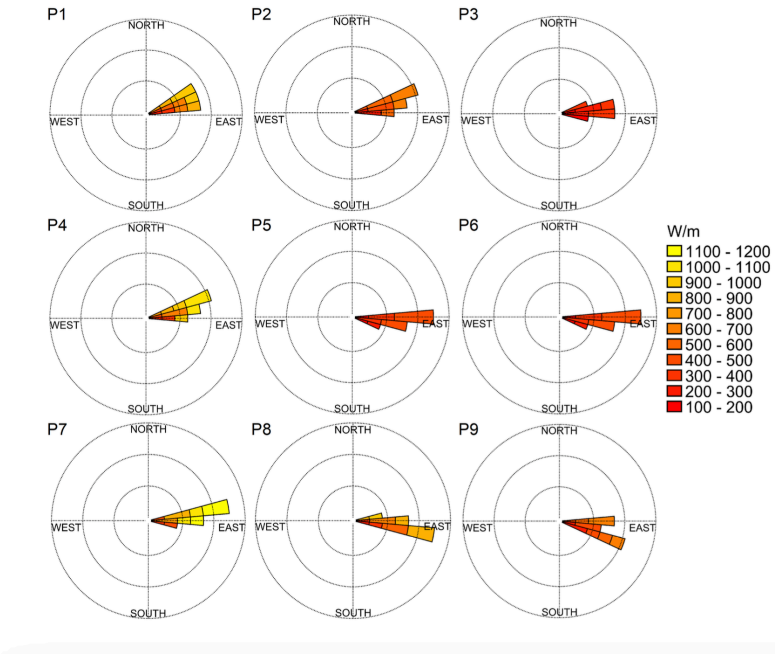

Fig. 11 Monthly mean WEF roses for the amplitudes shown in Figure 9, which correspond to the 9 zones displayed in Figure 8. Units in W/m.

coherence between 24 and 40 months is initially in phase for years 1964 and 1967, lagged (ENSO leads) between 1972 and 1974, and almost in phase between years 1978 and 1983. Regarding the periods between 24 and 92 months, the coherence is lagged (ENSO leads) from 1993 to 2017. The larger positive correlation between WEF and ONI found during El Niño events (either during Canonical or Modoki events, although is larger during Modoki ones) is likely caused by the strengthening of the CLLJ, especially in the Colombian basin (Wang 2007; García-Martínez and Bollasina 2020).

5 Conclusions

Departing from a 60-year wave simulation, the analysis features the spatial and temporal variability of the mean wave energy flux (WEF). First, we have performed a validation of the simulated significant wave height (H_s) and mean wave period (T_{m-01}), against *i*n-situ measurements from buoy 42058 of NOAA (Figure 2). Correlation, Weibull and Bias coefficients shown a good agreement between modeled and observed data. The database used here contributes to reduce the lack of available information of wave parameters in the Caribbean Sea (Orejarena-Rondón et al. 2021). Indeed such a simulation is the longest if compared to any other wave reanalysis available for the Caribbean Sea (Arias et al. 2009; Dagua et al. 2013; Appendini et al. 2015; Osorio et al. 2016), and it

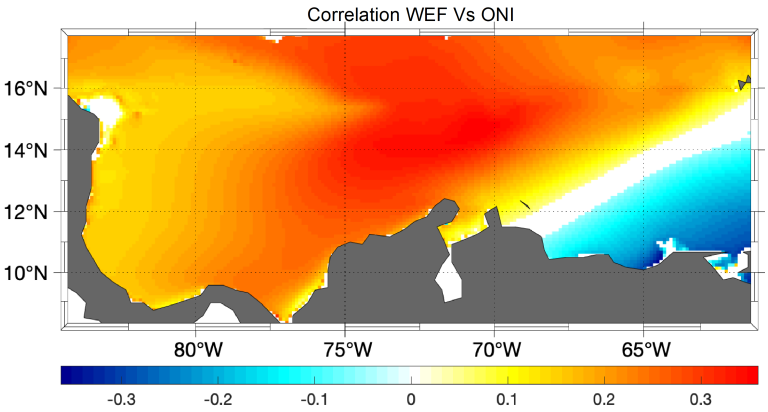

Fig. 12 Map of spatial correlation between monthly mean WEF and ONI for the study area. White color indicates a non statistically significant correlation. Red (blue) color indicate a positive (negative) correlation.

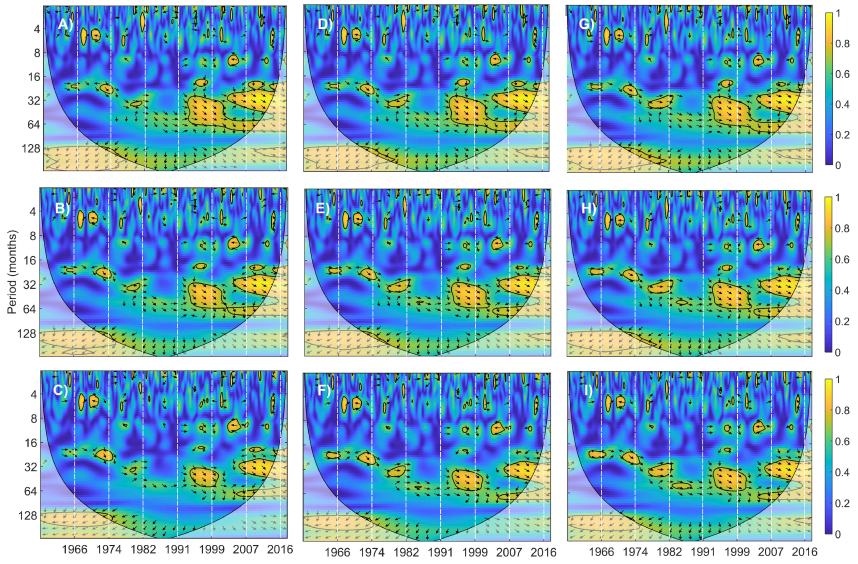

Fig. 13 Wavelet coherence (WTC) between monthly ONI and monthly mean WEF for all patterns provided by the temporal SOM analysis (Figure 8): (A) zone 1, (B) zone 2, (C) zone 3, (D) zone 4, (E) zone 5, (F) zone 6, (G) zone 7, (H) zone 8, and (I) zone 9. Arrows determine the phase between both series. Arrows pointing to the right represent positive correlation (in phase signals). Arrows pointing to the left represent anti-correlation (out of phase signals). Contours depict the wavelet squared coherence significant at 95%.

has already been employed for marine energy assessment (Orejarena-Rondón et al. 2022). However, this simulation can also be used for studies of coastal vulnerability, to analyze climate variability, or to study open sea extreme wave

conditions for coastal and offshore engineering, among other possible applications. The database is freely accessible in the repository `https://nimbus.imedea.uib-csic.es/s/JEaPEeeQNLPFJ3S` (Orejarena-Rondón et al. 2021). By applying a spatial SOM analysis over monthly mean WEF data it was possible to regionalize the WEF variability in the Caribbean Sea. Thus, WEF information was classified into 9 patterns that captured the complex behavior of WEF (magnitude and direction). A similar analysis was also performed for the surface horizontal wind. Results indicate that the behavior of mean WEF is strongly modulated by the wind seasonal variations, which in turn changes with the latitudinal migration of the Inter Tropical Convergence Zone (ITCZ) over the Caribbean basin (Andrade 1993; Andrade and Barton 2013; Poveda et al. 2006). Obtained patterns (P_i) with highest probability of occurrence are: P1 with 22.64% (dry season), the P6 with 17.36% (wet season) and the P7 with 14.58% (transition season), all of them associated with the growth of the wave height and the change in wave period of waves as they move westward, reaching the maximum for P1 off the Colombian coasts. Other patterns are less frequent and are distributed throughout the seasons: P4 and P2 occur during the dry season; P3 during the wet season (November); P5 and P8 occur during the transition season and in the beginning of the wet season. Finally, P9 occurs during both transition and wet seasons. As mentioned above, a SOM analysis was also applied to the surface winds used to force the model. Results are consistent with the 9 patterns obtained in the analysis of WEF (Figures 5 and 6, top panel). In this case, one observe greater influence of the Caribbean Low Level Jet (CLLJ) in the eastern side of the basin, between longitudes 68°W-78°W and latitudes 11°N - 18°N, which differs from the WEF influence zone (72°W-83°W, and 10°N-16°N). A plausible explanation is the large fetch in the Caribbean Sea, which allows wind waves some space to growth until they reach their most energetic state (Figures 5 and 6, top panels). Afterwards, we performed a temporal SOM analysis over the zonal and meridional component of WEF in the Caribbean Sea. As a result, one identified 9 zones of co-variability where WEF features different magnitudes and directions (Figures 10 and 11). Unsurprisingly, the zonal component is more energetic, due to the dominant trade winds. In particular, the most energetic zones are 7, 4, 1 and 8 (Figure 9 in the top panel). Regarding the meridional component, the most energetic zones are the 1, 4, 7 and 2. These results illustrate why the resultant direction points sometimes to the west (P1). On the other hand, departing from above time series of WEF we have computed the seasonal cycle by calculating the 60-year monthly mean of the zonal and meridional components, respectively. As a result, we get the seasonal cycle for each component and every region. Figure 10 illustrates the influence of ITCZ latitudinal displacements. Interestingly, the zonal component depicts a seasonal cycle with two peaks in all regions. However, the meridional component has one peak in the three regions located more to the north in the Caribbean Sea. The more energetic is the region the more clearly defined are the two peaks since the CLLJ, whose semi-annual cycle has been reported in previous works (Chunzai 2007; Orfila et al. 2021), has a stronger influence. As one could expect, the

two peaks are more visible in the meridional component in those zones below 12°N (zones 1, 4 and 2). This is consistent with the description by Andrade (1993); Andrade and Barton (2013); Poveda et al. (2006), who described that northernmost position of ITCZ is located between 10°N-12°N. Above of this latitude the direction of WEF differs, as shown in Figure 11 for zones 6, 8 and 9.

Next, we have explored the relationship between ENSO and WEF at interannual scales. The correlation analysis has shown a strong positive correlation in the central part of the basin (0.4), lower but still positive in the Gulf of Darien (0.1–0.2), and negative off Venezuela (−0.3 to −0.1, Figure 12). This behavior is consistent with the findings of Enfield and Mayer (1997); Huang et al. (2002), who determined that when the Pacific warm anomalies during an ENSO event reach their maximum at the end of the year, trade winds weaken over the eastern Caribbean Sea at a latitude between 10°N and 20°N, and extend until Africa, while in the western Caribbean Sea trade winds strengthen. Finally, to determine the periods and lag times of common variability between ENSO and WEF we have computed the Wavelet Coherence (WTC). Results suggested the existence of a statistical correlation between changes in ONI and WEF in different time periods, thus indicating that the monthly mean WEF is sensitive to changes in ENSO. All regions were correlated with the ONI for periods between 24 and 40 months during years 1964–1967, 1972–1974 and 1978–1983, characterized by the occurrence of large warm events in the eastern Pacific. This correlation occurs with the same phase in all periods, being larger between zones 4–9 (see Figure 13). Similarly, a strong correlation during years 1993–2017 is observed in all regions for periods that span from 24 to 92 months, especially in zones 1, 4 and 7.

Acknowledgments

A. Orfila thanks financial support from grant RTI2018-093941-B-C31 funded by MCIN/AEI/ 10.13039/501100011033 and by "ERDF A way of making Europe". A. Orejarena-Rondon was supported by COLCIENCIAS (Call 727) and POGO-SCORE Visiting fellowship at the Mediterranean Institute for Advanced Studies. Aurthors acknwoledge DIMAR (Dirección General Maritima from Colombia) for the wave parameters supplied for the model validation. J.M. Sayol thanks the joint funding received from the Generalitat Valenciana and the European Social Fund under grant APOSTD/2020/254.

References

Alvarez-León R, Aguilera-Quiñonez J, Andrade C, Nowak P (1995) Caracterizacion general de la zona de surgencia en la guajira colombiana. Boletin Academia Colombiana de Ciencias Exactas Fisicas y Naturales 19:679–694

Amador JA (1998) A climate feature of the tropical americas: the trade wind easterly jet. Topicos Meteorologicos y Oceanograficos 5(2):91–102

Andrade C (1993) Análisis de la velocidad del viento en el mar caribe. Boletín Científico CIOH pp 33–43, DOI 10.26640/01200542.13.33-43

Andrade C, Barton E (2013) Sobre la existencia de una celda atmosférica sobre el caribe y su efecto sobre las corrientes de ekman en el mar caribe suroccidental. Boletín Científico Centro de Investigaciones Oceanografías e Hidrográficas, Cartagena, Colombia 31:73–94

Andrade C, Thomas YF, Alexandre NL, Durand P, Anselme B (2013) Coastal flooding hazard related to swell events in cartagena de indias, colombia. Journal of Coastal Research 290:1126–1136, DOI 10.2112/JCOASTRES-D-12-00028.1

Appendini CM, Urbano-Latorre CP, Figueroa B, Dagua-Paz CJ, Torres-Freyermuth A, Salles P (2015) Wave energy potential assessment in the caribbean low level jet using wave hindcast information. Applied Energy 137:375 – 384, DOI https://doi.org/10.1016/j.apenergy.2014.10.038

Ardhuin F, Orfila A (2018) Wind Waves, In New Frontiers in Operational Oceanography, chap 14, pp 393–422. DOI 10.17125/gov2018.ch14

Arias A, Mesa J, Bernal G, Montoya M (2009) Reconstrucción de cuarenta años de datos de oleaje en el mar caribe colombiano empleando el modelo wwiii™ y diferentes fuentes de datos. Boletín Científico CIOH pp 37–56, DOI 10.26640/01200542.27.37$_$56

Arinaga RA, Cheung KF (2012) Atlas of global wave energy from 10 years of reanalysis and hindcast data. Renewable Energy 39(1):49–64, DOI https://doi.org/10.1016/j.renene.2011.06.039

Booij N, Ris RC, Holthuijsen LH (1999) A third-generation wave model for coastal regions: 1. model description and validation. Journal of Geophysical Research: Oceans 104(C4):7649–7666, DOI https://doi.org/10.1029/98JC02622

Canals Silander MF, García Moreno CG (2019) On the spatial distribution of the wave energy resource in puerto rico and the united states virgin islands. Renewable Energy 136:442 – 451, DOI https://doi.org/10.1016/j.renene.2018.12.120

Chunzai W (2007) Variability of the caribbean low-level jet and its relations to climate. Climate Dynamics 29(1):1432–0894, DOI 10.1007/s00382-007-0243-z

Cuttler MV, Hansen JE, Lowe RJ (2020) Seasonal and interannual variability of the wave climate at a wave energy hotspot off the southwestern coast of australia. Renewable Energy 146:2337 – 2350, DOI https://doi.org/10.1016/j.renene.2019.08.058

Dagua C, Lonin S, Urbano C, Orfila A (2013) Calibración del modelo swan y validación de reanálisis del oleaje en el caribe. Boletín Científico CIOH 31:13–28, DOI 10.26640/01200542.31.13$_$28

Dodet G, Bertin X, Taborda R (2010) Wave climate variability in the north-east atlantic ocean over the last six decades. Ocean Modelling 31(3):120 – 131, DOI https://doi.org/10.1016/j.ocemod.2009.10.010

Elshinnawy AI, Medina R, González M (2017) On the relation between the direction of the wave energy flux and the orientation of equilibrium beaches. Coastal Engineering 127:20–36, DOI https://doi.org/10.1016/j.coastaleng.2017.06.009

Enfield DB, Mayer DA (1997) Tropical atlantic sea surface temperature variability and its relation to el niño-southern oscillation. Journal of Geophysical Research: Oceans 102(C1):929–945, DOI https://doi.org/10.1029/96JC03296

Fiedler JW, Brodie KL, McNinch JE, Guza RT (2015) Observations of runup and energy flux on a low-slope beach with high-energy, long-period ocean swell. Geophysical Research Letters 42(22):9933–9941, DOI https://doi.org/10.1002/2015GL066124

García-Martínez IM, Bollasina MA (2020) Sub-monthly evolution of the caribbean low-level jet and its relationship with regional precipitation and atmospheric circulation. Climate Dynamics 54(9):4423–4440, DOI 10.1007/s00382-020-05237-y

Grinsted A, Moore J, Jevrejeva S (2004) Application of cross wavelet transform and wavelet coherence to geophysical time series. Nonlinear Processes in Geophysics 11, DOI 10.5194/npg-11-561-2004

Guillou N (2020) Estimating wave energy flux from significant wave height and peak period. Renewable Energy 155:1383–1393, DOI https://doi.org/10.1016/j.renene.2020.03.124

Guillou N, Lavidas G, Chapalain G (2020) Wave energy resource assessment for exploitation—a review. Journal of Marine Science and Engineering 8(9), DOI 10.3390/jmse8090705

Hanson H, Aarninkhof S, Capobianco M, Jiménez JA, Larson M, Nicholls RJ, Plant NG, Southgate HN, Steetzel HJ, Stive MJF, de Vriend HJ (2003) Modelling of coastal evolution on yearly to decadal time scales. Journal of Coastal Research 19(4):790–811

Hernández-Carrasco I, Solabarrieta L, Rubio A, Esnaola G, Reyes E, Orfila A (2018) Impact of hf radar current gap-filling methodologies on the lagrangian assessment of coastal dynamics. Ocean Science 14(4):827–847, DOI 10.5194/os-14-827-2018

Hernández-Carrasco I, Orfila A (2018) The role of an intense front on the connectivity of the western mediterranean sea: The cartagena-tenes front. Journal of Geophysical Research: Oceans 123(6):4398–4422, DOI https://doi.org/10.1029/2017JC013613

Hernández-Carrasco I, Alou-Font E, Dumont PA, Cabornero A, Allen J, Orfila A (2020) Lagrangian flow effects on phytoplankton abundance and composition along filament-like structures. Progress in Oceanography 189:102469, DOI https://doi.org/10.1016/j.pocean.2020.102469

Huang B, Schopf PS, Pan Z (2002) The enso effect on the tropical atlantic variability: A regionally coupled model study. Geophysical Research Letters 29(21):35–1–35–4, DOI https://doi.org/10.1029/2002GL014872

Iglesias G, López M, Carballo R, Castro A, Fraguela J, Frigaard P (2009) Wave energy potential in galicia (nw spain). Renewable Energy 34(11):2323–

2333, DOI https://doi.org/10.1016/j.renene.2009.03.030

Japan Meteorological Agency J (2013) Research data archive at the national center for atmospheric research, computational and information systems laboratory. urlhttps://doi.org/10.5065/D6HH6H41

Kobayashi S, Ota Y, Harada Y, Ebita A, Moriya M, Onoda H, Onogi K, Kamahori H, Kobayashi C, Endo H, Miyaoka K, Takahashi K (2015) The jra-55 reanalysis: General specifications and basic characteristics. Journal of the Meteorological Society of Japan 93:5–48, DOI 10.2151/jmsj.2015-001

Kohonen T (1982) Self-organized formation of topologically correct feature maps. Biological Cybernetics 43(3), DOI https://doi.org/10.1007/BF00337288

Komen GJ, Hasselmann S, Hasselmann K (1984) On the existence of a fully developed wind-sea spectrum. Journal of Physical Oceanography 14(8):1271 – 1285, DOI 10.1175/1520-0485(1984)014⟨1271:OTEOAF⟩2.0.CO;2

Ponce de León S, Orfila A, Simarro G (2016) Wave energy in the Balearic Sea. Evolution from a 29 year spectral wave hindcast. Renewable Energy 85(C):1192–1200, DOI 10.1016/j.renene.2015.07.

Liang B, Shao Z, Wu G, Shao M, Sun J (2017) New equations of wave energy assessment accounting for the water depth. Applied Energy 188:130–139, DOI https://doi.org/10.1016/j.apenergy.2016.11.127

Liberti L, Carillo A, Sannino G (2013) Wave energy resource assessment in the mediterranean, the italian perspective. Renewable Energy 50:938–949, DOI https://doi.org/10.1016/j.renene.2012.08.023

Lin Y, Dong S, Wang Z, Guedes Soares C (2019) Wave energy assessment in the china adjacent seas on the basis of a 20-year swan simulation with unstructured grids. Renewable Energy 136:275 – 295, DOI https://doi.org/10.1016/j.renene.2019.01.011

Mentaschi L, Vousdoukas MI, Voukouvalas E, Dosio A, Feyen L (2017) Global changes of extreme coastal wave energy fluxes triggered by intensified teleconnection patterns. Geophysical Research Letters 44(5):2416–2426, DOI https://doi.org/10.1002/2016GL072488

Mirzaei A, Tangang F, Juneng L (2015) Wave energy potential assessment in the central and southern regions of the south china sea. Renewable Energy 80:454–470, DOI https://doi.org/10.1016/j.renene.2015.02.005

Morales V, Hernández-Carrasco I, Fox-Kemper B, Orfila A (2022) Ageostrophic contribution by the wind and waves induced flow to the lateral stirring in the mediterranean sea. EarthArXiv DOI 10.31223/X56D25

Morales-Márquez V, Hernández-Carrasco I, Simarro G, Rossi V, Orfila A (2021) Regionalizing the impacts of wind- and wave-induced currents on surface ocean dynamics: A long-term variability analysis in the mediterranean sea. Journal of Geophysical Research: Oceans 126(9):e2020JC017104, DOI https://doi.org/10.1029/2020JC017104, e2020JC017104 2020JC017104

Nalley D, Adamowski J, Khalil B, Biswas A (2016) Inter-annual to inter-decadal streamflow variability in quebec and ontario in relation to dominant large-scale climate indices. Journal of Hydrology 536:426–446, DOI

https://doi.org/10.1016/j.jhydrol.2016.02.049
Orejarena-Rondón AF, Orfila A, Restrepo JC, Ramos IM, Hernandez-Carrasco I (2021) A 60 year wave hindcast dataset in the southern caribbean sea. Data in Brief p 107153, DOI https://doi.org/10.1016/j.dib.2021.107153
Orejarena-Rondón AF, Restrepo JC, Correa-Metrio A, Orfila A (2022) Wave energy flux in the caribbean sea: Trends and variability. Renewable Energy 181:616–629, DOI https://doi.org/10.1016/j.renene.2021.09.081
Orfila A, Urbano-Latorre CP, Sayol JM, Gonzalez-Montes S, Caceres-Euse A, Hernández-Carrasco I, Muñoz AG (2021) On the impact of the caribbean counter current in the guajira upwelling system. Frontiers in Marine Science 8:128, DOI 10.3389/fmars.2021.626823
Ortega S, Osorio AF, Agudelo P (2013) Estimation of the wave power resource in the caribbean sea in areas with scarce instrumentation. case study: Isla fuerte, colombia. Renewable Energy 57:240–248, DOI https://doi.org/10.1016/j.renene.2012.11.038
Ortiz-Royero JC, Mercado-Irizarry A (2008) An intercomparison of swan and wavewatch iii models with data from ndbc-noaa buoys at oceanic scales. Coastal Engineering Journal 50(1):47–73, DOI 10.1142/S0578563408001739
Osorio A, Ortega Arango S, Arango-Aramburo S (2015) Assessment of the marine power potential in colombia. Renewable and Sustainable Energy Reviews 56:966–977, DOI 10.1016/j.rser.2015.09.057
Osorio AF, Montoya RD, Ortiz JC, Peláez D (2016) Construction of synthetic ocean wave series along the colombian caribbean coast: A wave climate analysis. Applied Ocean Research 56:119–131, DOI https://doi.org/10.1016/j.apor.2016.01.004
Poveda G (2004) La hidroclimatología de colombia: Una síntesis desde la escala inter-decadal hasta la escala diurna. Rev Acad Colomb Cienc 28:201–222
Poveda G, Mesa O (1999) La corriente de chorro superficial del oeste ("del chocó") y otras dos corrrientes de chorro atmosféricas sobre colombia: Climatología y variabilidad durante las fases del enso. Revista de la Academia Colombiana de Ciencias Exactas Fisicas y Naturales 23:517–528
Poveda G, Waylen PR, Pulwarty RS (2006) Annual and inter-annual variability of the present climate in northern south america and southern mesoamerica. Palaeogeography, Palaeoclimatology, Palaeoecology 234(1):3–27, DOI https://doi.org/10.1016/j.palaeo.2005.10.031, late Quaternary climates of tropical America and adjacent seas
Reguero B, Losada I, Méndez F (2015) A global wave power resource and its seasonal, interannual and long-term variability. Applied Energy 148:366–380, DOI https://doi.org/10.1016/j.apenergy.2015.03.114, URL https://www.sciencedirect.com/science/article/pii/S030626191500416X
Reguero B, Losada I, Méndez F (2019) A recent increase in global wave power as a consequence of oceanic warming. Nature Communications 10, DOI 10.1038/s41467-018-08066-0
Restrepo JC, Higgins A, Escobar J, Ospino S, Hoyos N (2019) Contribution of low-frequency climatic–oceanic oscillations to streamflow variability

in small, coastal rivers of the sierra nevada de santa marta (colombia). Hydrology and Earth System Sciences 23(5):2379–2400, DOI 10.5194/hess-23-2379-2019, URL https://hess.copernicus.org/articles/23/2379/2019/

Richardson A, Risien C, Shillington F (2003) Using self-organizing maps to identify patterns in satellite imagery. Progress in Oceanography 59(2):223–239, DOI https://doi.org/10.1016/j.pocean.2003.07.006, eNVIFISH: Investigating environmental causes of pelagic fisheries variability in the SE Atlantic

Rivera-Páez S, Molares R (2003) Evidencias de la oscilación del tiempo madden y julian en el caribe colombiano. Boletín Científico CIOH pp 101–113, DOI 10.26640/01200542.21.101$_$113

Sayol JM, Vasquez LM, Valencia JL, Linero-Cueto JR, Garcia-Garcia D, Vigo I, Orfila A (2022) Extension and application of an observation-based local climate index aimed to anticipate the impact of el niño–southern oscillation events on colombia. International Journal of Climatology n/a(n/a), DOI https://doi.org/10.1002/joc.7540

van Vledder GP (2006) The wrt method for the computation of non-linear four-wave interactions in discrete spectral wave models. Coastal Engineering 53(2):223–242, DOI https://doi.org/10.1016/j.coastaleng.2005.10.011, coastal Hydrodynamics and Morphodynamics

Wang C (2007) Variability of the caribbean low-level jet and its relations to climate. Climate Dynamics 29(4):411–422, DOI 10.1007/s00382-007-0243-z

Waters R, Engström J, Isberg J, Leijon M (2009) Wave climate off the swedish west coast. Renewable Energy 34(6):1600–1606, DOI https://doi.org/10.1016/j.renene.2008.11.016

Wiggins M, Scott T, Masselink G, Russell P, McCarroll RJ (2019) Coastal embayment rotation: Response to extreme events and climate control, using full embayment surveys. Geomorphology 327:385–403, DOI https://doi.org/10.1016/j.geomorph.2018.11.014

Wu L, Qin J, Wu T, Li X (2017) Trends in global ocean surface wave characteristics as represented in the era-interim wave reanalysis for 1979–2010. Journal of Marine Science and Technology 23, DOI 10.1007/s00773-017-0450-1